Fabrication of nanopores with embedded annular electrodes and transverse carbon nanotube electrodes

2010 J. Phys.: Condens. Matter 22 454114

(http://iopscience.iop.org/0953-8984/22/45/454114)

IOP Publishing Journal of Physics: Condensed Matter

J. Phys.: Condens. Matter **22** (2010) 454114 (10pp) doi:10.1088/0953-8984/22/45/454114

Fabrication of nanopores with embedded annular electrodes and transverse carbon nanotube electrodes

Zhijun Jiang, Mirna Mihovilovic, Jason Chan and Derek Stein

Department of Physics, Brown University, Providence, RI, 02912, USA

E-mail: derek_stein@brown.edu

Received 6 April 2010, in final form 7 May 2010
Published 29 October 2010
Online at stacks.iop.org/JPhysCM/22/454114

Abstract

Nanopores with one or two embedded nanoelectrodes can be fabricated by high resolution, milling-based methods. We first demonstrate how a focused ion beam, whose sputtering mechanism is well understood, can create a nanopore containing an annular electrode of an arbitrary metal, and with a regular perimeter. The inner surface of the nanopore can be insulated, and its diameter can be reduced with nanometer precision, by conformally coating a dielectric material by atomic layer deposition. We then investigate the mechanism of pore formation using a transmission electron microscope (TEM) through studies of the milling rate, and its dependence on the flux of electrons and on the atomic number of different target metals. Sputtering from the surface is identified as the dominant mechanism. Accordingly, light element conductors should be chosen to enhance the rate and resolution of TEM milling, which we demonstrate by articulating a nanopore with transverse carbon nanotube electrodes. Finally, we electrochemically verify that TEM milling preserves the quality of an annular gold electrode through cyclic voltammetry measurements performed at various stages of the fabrication.

(Some figures in this article are in colour only in the electronic version)

1. Introduction

The development of solid-state nanopores for electrical DNA sensing was strongly motivated by the prospect of incorporating nanoelectrodes [1]. The functionality of a synthetic nanopore fabricated by top-down methods can be enhanced by a gate electrode or by local sensing electrodes that are not available in passive biological pores like α-hemolysin. For example, an embedded annular electrode can gate the surface charge density inside the pore, thereby influencing the transport of ions [2–4] and possibly also the capture and transport of molecules like DNA via the electrofluidic field effect [5]. Alternatively, an exposed electrode inside a nanopore could serve as a sensor for monitoring the local electrochemical potential. A nanopore decorated by a pair of transverse electrodes was even put forward as a potential DNA sequencing device [6, 7], with which the translocating bases could be electrically discriminated via the tunneling current [6–10]. Motivated by these and other possibilities, recent work has focused on integrating electrode materials into nanopores [11–15].

A leading technique for creating nanopores in insulating materials such as silicon nitride and silicon dioxide employs the highly focused beam of a transmission electron microscope (TEM) to mill directly through a thin, freestanding membrane [16–18]. Nanopores with diameters as small as a single nanometer can be achieved [19, 20]. The ability of TEM to image while milling is another attractive capability, in principle enabling a precisely aligned pore to be created through a patterned electrode structure. The application of TEM milling to metals has resulted in remarkable electronic nanostructures, however achieving single nanometer resolution is complicated by the propensity of materials such as gold to diffuse and recrystallize when exposed to the TEM beam [11, 13]. Importantly, the microscopic mechanisms responsible for the formation of pores in a TEM are not fully understood, making it difficult to rationally improve the technique. Furthermore, the electrical properties of the surface in contact with solution after TEM processing remain unclear.

Here we develop high resolution, milling-based methods for articulating nanopores with one or two nanoelectrodes. The basic strategy is to embed a conducting material in an

insulating, freestanding membrane, and then to mill through the heterostructure so as to expose the electrode on the inner surface of the nanopore. We first use a focused ion beam (FIB) to create an annular electrode inside a nanopore. The sputtering mechanism of FIB is well understood, and it allows a regular perimeter to be defined in nearly any electrode material. Embedded annular electrodes fabricated by FIB can be insulated with a dielectric, and are well suited for controlling the flow of ions or DNA molecules through the nanopore. The principal drawback of FIB is that its spatial resolution is insufficient to define pores or gaps between electrodes at the single nanometer scale, which is desired for certain electronic DNA interrogation strategies.

We then study the TEM milling process, which has the potential to achieve single nanometer resolution. The flux dependence of the TEM-induced milling rate and the dependence of the milling rate through thin metal films on the atomic number of the target both point to sputtering from the surface as the dominant mechanism of pore formation. This insight instructs the choice of a light element conductor like graphitic carbon, for which the sputtering yield by electrons is enhanced. We demonstrate that a TEM can be used to locate and bisect an embedded carbon nanotube with relative ease. This approach results in a pair of transverse CNT electrodes flanking the inner surface of a TEM-milled nanopore, which may be useful for probing the electronic properties of confined molecules. It is important for such electronic sensing that the TEM milling process preserve the electrical properties of the embedded electrode surface. We finally use electrochemical measurements to verify the conductance at the interface between electrolyte and an annular gold electrode embedded inside a TEM-milled nanopore.

2. Fabrication of freestanding membranes with patterned electrodes

The starting point for creating nanopores with embedded electrodes is a thin, freestanding membrane of silicon nitride suspended over a silicon substrate. We fabricated such structures following a procedure, described below, that was inspired by Krapf *et al* [21]. An important distinction is that the 20 nm thick silicon nitride membrane that hosts the nanopore is the uppermost material layer in our devices. This ordering provides a flat membrane surface onto which electrodes can be easily patterned by standard lithography. A sketch of the cross-sectional layout of the device structure is shown in figure 1(a).

The freestanding membrane structures were formed from the following material stack: 400 nm of low stress (silicon rich) silicon nitride (SiN) were first deposited on both sides of a 400 μm thick silicon substrate by low pressure chemical vapor deposition (LPCVD). 400 nm of SiO_2 were then deposited on the front side by plasma enhanced chemical vapor deposition (PECVD), followed by another 20 nm of SiN deposited on both sides. Photolithography was used to expose a pattern of 760 μm wide squares on the back side, which was then transferred into the silicon substrate by etching in a reactive plasma of CF_4. Wet anisotropic etching of the silicon (KOH 40 wt%, 70 °C) resulted in 200 μm wide square membranes

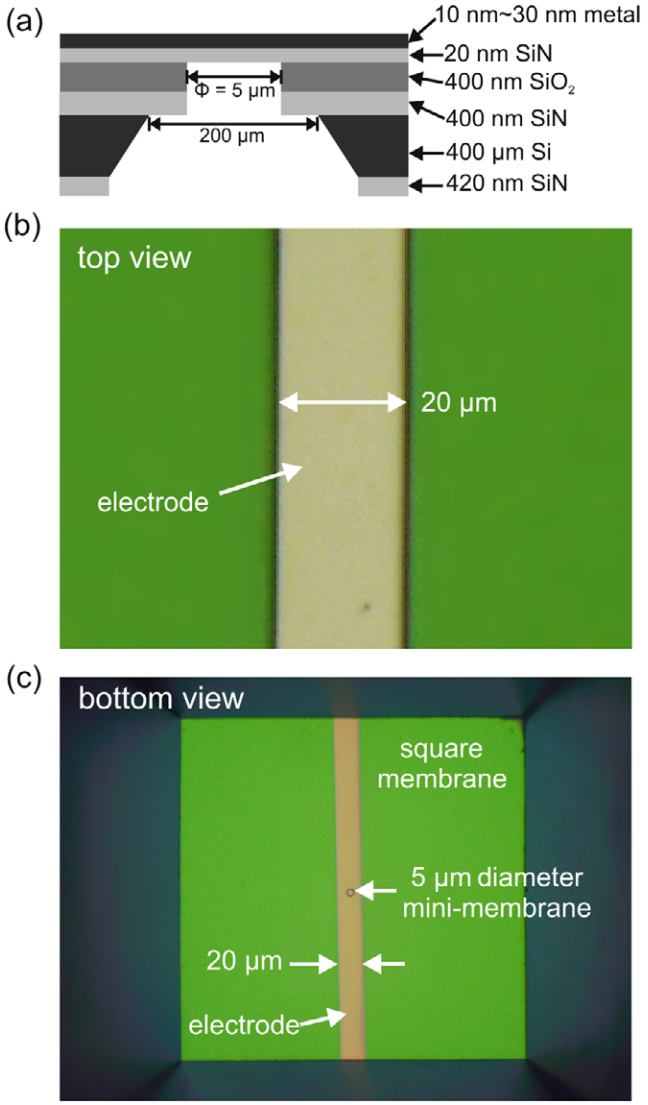

Figure 1. Patterned metal electrodes on a freestanding membrane. (a) Illustration of the device cross-section. (b) Optical micrograph showing the wide square membrane and the electrode from the top. (c) Optical micrograph showing the wide square membrane from the bottom. The 5 μm diameter mini-membrane is visible.

suspended on the front side. A FIB was used to mill through the 400 nm thick SiN layer from the back, forming a 5 μm diameter pit in the center of the square membrane that exposed the underlying SiO_2 layer. That SiO_2 was then sacrificially etched in buffered hydrofluoric acid. The etch terminated at the 20 nm thick SiN layer, leaving a circular mini-membrane into which the nanopore would be milled.

Patterned electrodes were deposited on the flat, front surface of our devices using standard photolithography and metal evaporation. Figures 1(b) and (c) show optical micrographs of the front and back surfaces of the wide square membranes, across which a 20 μm wide gold electrode was defined. The electrode joined two wide contact pads located at opposite corners of the 5 mm square nanopore chip. This design allowed the integrity of the electrode to be verified at any stage of processing by measuring its conductance.

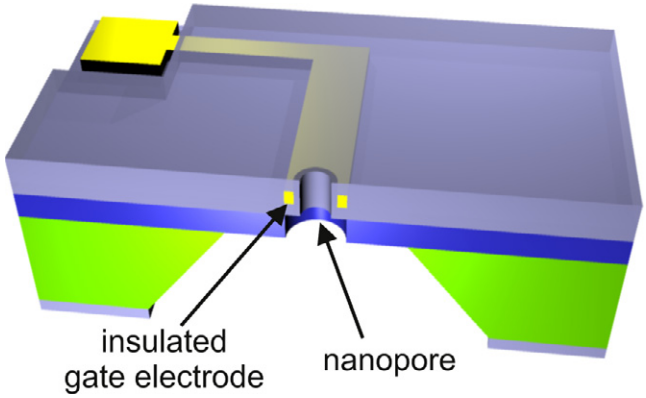

Figure 2. Illustrated cross-section of a gated nanopore device containing an embedded and insulated electrode. The gate electrode can be used to modulate the potential at the inner surface of the nanopore.

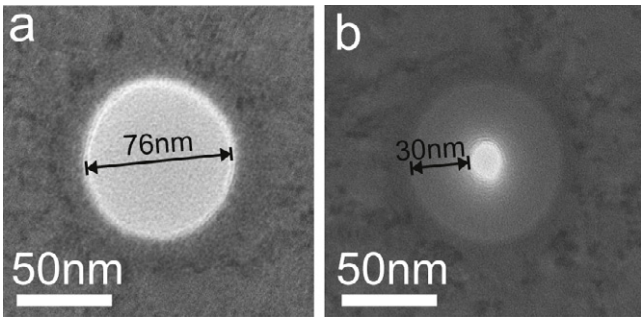

Figure 3. A nanopore with an embedded gate electrode. TEM images of (a) a 76 nm diameter nanopore milled through a 30 nm thick Cr electrode on a 20 nm thick SiN membrane using FIB, and (b) the same nanopore after depositing 30 nm of Al_2O_3 by ALD. The final diameter of the nanopore was 16 nm.

3. Fabricating an embedded gate electrode in a nanopore by FIB milling

A FIB directs a finely focused beam of massive ions (typically Ga^+) onto a solid target at kiloelectronvolt energies. Atomic sputtering locally erodes the incident surface, permitting sharp features to be defined in metals, semiconductors and insulators, with critical dimensions in the tens of nanometers [22, 23]. It is consequently straightforward to mill through a stack of materials so as to incorporate an annular electrode inside an insulating nanopore. We are interested in creating the electrically gated nanopore structure illustrated in figure 2, in which a single nanopore is surrounded by an embedded electrode whose surface is protected by a thin gate dielectric. Such gated nanopores are designed to control the passage of ions and DNA molecules using the electrofluidic field effect.

Figure 3(a) shows a 76 nm diameter nanopore produced by FIB milling through a 30 nm thick chromium electrode on a 20 nm thick SiN mini-membrane. The FIB (Zeiss NVision 40) employed a 10 pA beam of 30 keV Ga^+, impinging at normal incidence on the back surface. The perimeter of the pore appears circular and smooth. We have fabricated similar structures using a variety of electrode materials, including Cr, Au, Ti, and Al, with the electrode thicknesses ranging from 10 to 100 nm. Circular nanopores with smooth perimeters could always be produced within seconds by FIB milling.

The electrode surface can be insulated, and the pore diameter can be finely tuned, by growing a thin dielectric layer using atomic layer deposition (ALD). Figure 3(b) shows the same pore as in figure 3(a) after 30 nm of Al_2O_3 was grown by ALD at 300 °C using water vapor and trimethylaluminum as precursor gases. The average thickness of the Al_2O_3 layer measured from the electrode perimeter was 29.6 nm, and diameter of the nanopore was reduced to 16 nm, as intended. The final diameter of ALD-coated nanopores can regularly be specified to within a nanometer based on the known deposition rate and the initial diameter of the pore, as measured by TEM. Such high accuracy is possible because ALD is an epitaxial growth process that coats surfaces conformally [24, 25].

The ability of FIB to mill quickly through an arbitrary material derives from the sputtering mechanism by which atoms are ejected from the surface and the near surface of the target [26]. The sputter yield, defined as the number of atoms ejected per incident ion, is high (typically >2) for 30 keV Ga^+ impinging on most materials because the incident ion can transfer much of its kinetic energy to a target atom, and thereby overcome the surface binding energy, E_s, or the bulk displacement energy, E_d. Modeling the interaction between an incident ion and a target atom as an elastic two-body collision, the maximum transferrable energy, E_{max}, is found to be [27]:

$$E_{max} = \frac{4M_1M_2}{(M_1+M_2)^2}E_0, \qquad (1)$$

where E_0 is the kinetic energy of the incident particle, and M_1 and M_2 are the masses of the incident ion and the target atom, respectively. Equation (1) indicates that the incident kinetic energy can be most efficiently transferred to the target when the masses of the incident and target atoms are closely matched. Nevertheless, hundreds to thousands of electronvolt are transferred in typical collisions with 30 keV Ga^+ ions, even for targets with dissimilar masses.

Although the sputtering process makes FIB milling effective, it also limits the spatial resolution that can be achieved. The 30 keV energy of incident Ga^+ ions from an FIB greatly exceeds E_s and E_d, which are typically several electronvolt. A single incident ion therefore generates a cascade of collisions within the target, in which many atoms become displaced or sputtered [23]. The lateral extent of the collision cascade is typically about 10 nm. Milling structures with critical dimensions in the single nanometer range is consequently difficult.

4. Investigations into the mechanism of pore creation in a TEM

The rearrangement of matter by energetic electron beams has been studied for many years, beginning with the observed pitting of Au(111) surfaces by megaelectronvolt electrons [28]. A wide range of electron energies, electron

fluxes, and target materials have been studied, and a number of different microscopic transport processes have been considered, including atomic displacement [29–31], surface sputtering [13, 28, 31–34], stimulated atomic rearrangements by diffusion or viscous flow [11, 17, 18, 28, 30, 32, 34, 35], crystallization [11, 13, 31], charging [35, 36], and heating [36, 37] followed by subsequent vaporization [38]. Most of these studies identified sputtering and stimulated diffusion as the dominant transport mechanisms, which are both induced by elastic electron scattering off the target nucleus [39]. Nuclear scattering also generates vacancies and defects in the target, which can lead to recrystallization via diffusion. Inelastic scattering off the bound electrons of the target atoms can lead to charging (by electron ejection) and heating (by thermal relaxation of excited electrons) in the material [39], however the importance of such processes is thought to be small or insignificant [31, 35].

TEM milling is now widely used to fabricate solid-state nanopores for DNA translocation studies, so understanding the microscopic mechanism is becoming increasingly important. However, most studies have focused on how an electron beam can modify the size of an existing nanopore. For example, Storm *et al* proposed that irradiation of SiO_2 nanopores by an intermediate flux (10^5–10^7 e^- nm^{-2} s^{-1}) of 200 keV electrons fluidized the material, leading to surface-energy-driven material flows [18, 40]. This mechanism was supported by Kim *et al* [41]. The mechanism by which a TEM initially creates a nanopore has not been extensively examined. Here we investigate those mechanism through studies of the flux dependence of the milling rate, and its dependence on the atomic number of the target material. Our goal is to understand the TEM milling process so that it can be optimized for the fabrication of nanopores articulated with nanoelectrodes.

4.1. The flux dependence of the TEM milling rate

We measured the flux dependence of the milling rate of a 200 keV electron beam incident on 20 nm thick, freestanding SiN mini-membranes. The experiments were performed using a JEOL 2010 field emission TEM. The milling rate was established by condensing the focused beam of electrons onto the mini-membrane, and measuring the time required to mill through the material and create a nanopore. The incident electron current density was first established by dividing the measured beam current by the size of the condensed spot, as measured on the phosphorous screen of the TEM at a magnification of 800 000×. The measured electron flux was 2.6×10^8 e^- nm^{-2} s^{-1}. The electron flux was then varied by adjusting the beam condenser to obtain the same spot size on the phosphorous screen at lower values of the TEM magnification, assuming the beam profile and beam current were unchanged. This approach ensured that the relative magnitudes of the electron flux would be accurately known, even though determining the absolute electron flux of an electron beam with a Gaussian profile is challenging. The milling rate was measured seven times for each flux at different locations on the same SiN mini-membrane.

The flux dependence of the mean measured milling rate is shown in figure 4. A linear increase in the milling rate of

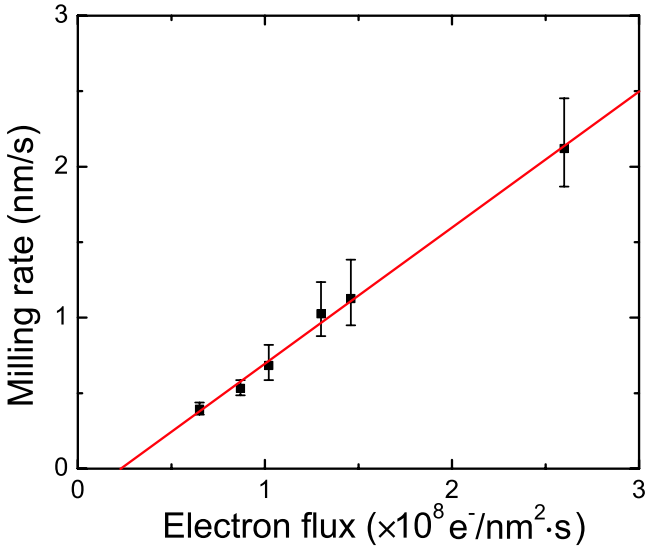

Figure 4. The electron flux dependence of the SiN nanopore milling rate in a 200 keV electron beam. The error bars correspond to the standard deviation of the milling rate measured at each electron flux. The line is a linear fit to the milling rate data that extrapolates to zero when $J = 2 \times 10^7$ e^- nm^{-2} s^{-1}.

SiN by 200 keV electrons as a function of the electron flux was observed beyond a threshold flux, J_{th}, as can be seen from the linear fit to the experimental data. The milling rate intercepted the flux axis at $J_{th} = 2 \times 10^7$ e^- nm^{-2} s^{-1}.

The linear increase in the milling rate with flux is consistent with the sputtering of atoms from the surface. The fact that the milling rate extrapolates to zero for a finite value of J_{th} suggests that there is a competition between sputter-dominated milling and the lateral, surface-tension-driven transport of matter responsible for the shrinking of pores at low fluxes [18]. This interpretation is consistent with the value of J_{th} measured here, which falls between the typical electron fluxes used for milling ($\sim 10^8$ e^- nm^{-2} s^{-1}) and for shrinking ($\sim 10^6$ e^- nm^{-2} s^{-1}) nanopores [18, 41].

4.2. TEM milling though different metals

TEM milling offers a promising route towards incorporating electrodes into nanometer scale pores. We have consequently studied the TEM milling process on a variety of different metals films, deposited on ≈25 nm thick amorphous carbon TEM support grids (electron microscopy sciences) by thermal evaporation. The materials tested included 50 nm thick films of Al, Cr, Fe, Co, Ni, and Cu, as well as Ti (2 nm)/Ag (8 nm) and Ti (2 nm)/Sn (8 nm) stacks. In addition, Ti (10 nm) and Ti (2 nm)/Au (8 nm) films were evaporated on 20 nm thick SiN membranes.

We succeeded in milling nanopores through each of the 10 metal films listed above using a high electron beam flux of $\approx 2.6 \times 10^8$ e^- nm^{-2} s^{-1}. Figure 5 presents representative TEM images of the resulting nanopores, arranged in order of increasing atomic number of the metal film. Note that perimeter of the nanopores tended to grow increasingly irregular, as did the apparent thickness of the surrounding

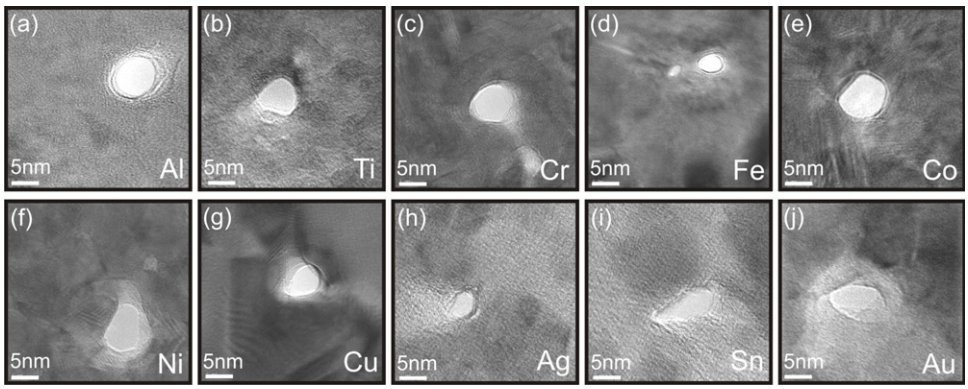

Figure 5. Nanopores fabricated in various metals by TEM milling. (a) Al, (b) Ti, (c) Cr, (d) Fe, (e) Co, (f) Ni, (g) Cu, (h) Ag, (i) Sn and (j) Au.

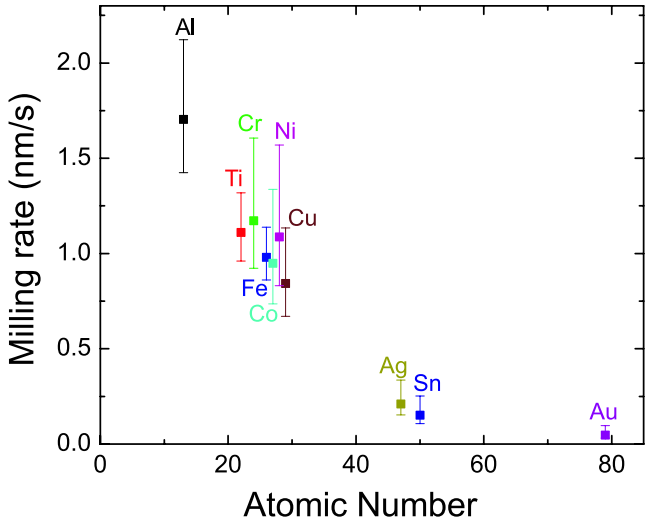

Figure 6. The milling rate for different metals under 200 keV electron beam. The milling rate decreases with increasing atomic number. The beam intensity was $\approx 2.6 \times 10^8$ e$^-$ nm^{-2} s^{-1}.

material (judged by variations in the transmitted electron density), as the atomic number increased.

The TEM milling rate depended on the type of metal film, decreasing strongly for heavier metals. Figure 6 plots the mean measured milling rate as a function of the atomic number of the metal target for the high beam intensity $J \approx 2.6 \times 10^8$ e$^-$ nm^{-2} s^{-1}. In determining the time to form nanopores through the metal films, we accounted for the time required to mill through the substrates. The milling rates of the carbon support and the SiN substrate were measured to be 6 nm s^{-1} and 2 nm s^{-1}, respectively, which was fast compared with the milling rates through the metal films.

The target-dependent TEM milling rates we measured are consistent with the sputter erosion mechanism. Since the incident electrons are very light, they are much less effective at transferring their kinetic energy to the atoms in the target material than the ions used in an FIB. The maximum transferrable energy in an elastic electron–atom collision (the equivalent of equation (1) for incident electrons) is given by [42]:

$$E_{\max} = 2E_0(E_0 + 2m_e c^2)/Mc^2, \tag{2}$$

where m_e is the mass of the electron, M is the mass of the target atom, and c is the speed of light. Equation (2) shows that $E_{\max}$ is inversely related to the atomic number of the metal target. Accordingly, we expect the rate of a TEM milling process dominated by sputtering to be inversely related to the atomic number, as was observed.

Table 1. Comparison of the surface binding energy, the displacement energy, and the maximum transferrable energy by 200 keV electrons for 10 metals. The E_s and E_d values are taken from [43], except for Sn [44].

Element	Al	Ti	Cr	Fe	Co	Ni	Cu	Ag	Sn	Au
$E_{\max}$ (eV)	19.3	10.8	10.0	9.33	8.84	8.87	8.20	4.83	4.39	2.65
E_s (eV)	4–8	4–8	5–11	4–8	5–12	6–11	4–9	7–14	—	9–18
E_d (eV)	16	15	22	16	23	22	18	28	22	36

In order to further assess the importance of sputtering and of atomic displacements by 200 keV electrons, table 1 compares the predicted values of $E_{\max}$ with the known values of E_s and E_d for the different metals tested. $E_{\max}$ only exceeds E_d for the lightest metal, Al, therefore atomic displacements in the bulk are expected to play a relatively minor role in the formation of pores. E_s is generally lower than E_d because surface atoms are bound by fewer bonds than bulk atoms, therefore sputtering from the surface is expected to dominate. We note that $E_{\max}$ is lower than E_s for metals heavier than Cu, so the formation of pores in Ag, Sn, and Au may be the result of a two-electron ejection process.

Other effects induced by TEM exposure such as electrostatic charging and heating are insignificant for metals. The high electric conductivity of metal films precludes electrostatic charging, and their relatively high thermal conductivities ensures that the local temperature rise caused by an intense TEM electron beam does not exceed a few kelvin [39].

Finally, we note that our observation of higher TEM milling rates for light target elements, including the carbon and SiN substrates, was inconsistent with the observations of Fischbein *et al*, who reported faster milling of Au electrodes

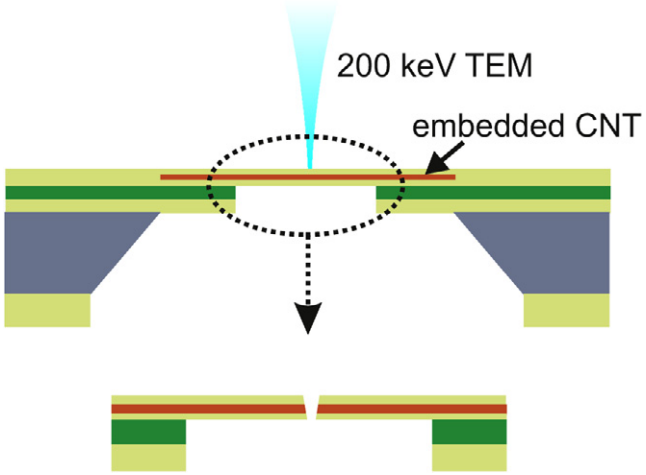

Figure 7. Schematic of the fabrication of a nanopore with transverse CNT electrodes.

than their SiN support membranes [13]. We speculate that this apparent discrepancy may be explained by differences in the location of the TEM focal plane in each experiment. Since a TEM has a narrow depth of field (≈10 nm) [43], a beam focused in the plane of the electrodes would have a much higher intensity there than within the ∼40 nm thick SiN membranes used by Fischbein *et al*.

5. Articulating a nanopore with transverse CNT electrodes

We infer from our studies of TEM milling that sputtering should be promoted in order to optimize the fabrication of nanopores. A high sputter yield translates into fast milling, and the possibility of defining predictable pore perimeters at high resolution. The theory of sputtering by electrons, through equation (2), predicts that sputtering is enhanced for the electron bombardment of light elements. We consequently reason that heavy metals such as gold are poorly suited for forming nanoelectrodes at high resolution. Instead, we hypothesize that a conductor made of a light elements, such as a carbon nanotube, should be easily milled in a TEM.

Here, we demonstrate that a carbon nanotube embedded in a freestanding membrane can be directly imaged and then bisected in a TEM. The resulting structure is a nanopore decorated with transverse CNT electrodes. A schematic illustration of the fabrication procedure is shown in figure 7.

Single walled CNTs (Nanostructured & Amorphous Materials, TX, USA) were suspended in ethanol by sonicating for 1 h. A 2 μl drop of the CNT suspension was deposited on front side of a chip containing an array of 20 nm thick SiN mini-membranes, and then left to dry at room temperature. The locations of individual CNTs were determined by imaging the mini-membranes in a TEM. The CNTs were then covered by a 20 nm thick layer of SiN, deposited on the front side of the device by PECVD (at 320 °C, using NH_3 and SiH_4 as the process gases). TEM imaging was again used to locate the same CNTs that were identified prior to the SiN deposition.

Figures 8(a) and (c) show two CNTs embedded inside a SiN mini-membrane prior to TEM milling. The diameters of the CNTs were 3 nm and 4 nm, respectively. The locations, orientations, and diameters of the embedded CNTs were the same as had been observed for the newly deposited CNTs, and they remained continuous, suggesting that they survived the deposition of SiN by PECVD. Additional electrical transport measurements would be needed to unambiguously verify the integrity and electrical properties of the CNTs. Such measurements were not performed because of the added complexity associated with electrically contacting the CNTs. Our main goal here was to demonstrate the resolution and feasibility of this fabrication technique, and to illustrate the benefits of an ability to both image and mill embedded electrodes in a TEM.

Nanopores were milled through embedded CNTs by condensing the electron beam on them. We were able to continuously observe a CNT in the low intensity tails (forming a triangular halo) around the high intensity center of the beam. The alignment of the electron beam on the CNT was maintained in real time using the fine beam-shift knobs of the TEM instrument. Figures 8(b) and (d) show the same nanotubes as figures 8(a) and (c) after TEM milling. The oval nanopore in figure 8(b) resulted in a 12 nm gap between the ends of the CNT. The more circular nanopore in figure 8(d) resulted in a 9 nm gap between the CNT electrodes. Although maintaining proper alignment of the beam and a CNT required skill on the part of the TEM operator, we successfully bisected two embedded CNTs out of the first five we attempted. Failed attempts resulted in misaligned nanopores that only partially cut the CNT. Milling through SiN mini-membranes with embedded CNTs proceeded as quickly as milling through the mini-membrane alone, as expected.

A CNT can be either metallic or semiconducting, depending on its chirality [45]. Typically, two thirds of randomly grown CNTs are semiconducting, while one third are metallic. The band structure of a transverse CNT pair is expected to influence its performance as an electrical probe of a translocating biomolecule. Theoretical explorations of electronic DNA sequencing have all modeled metallic electrodes [8, 9, 46], and scanning tunneling microscopy studies have used metal tips to probe the structure of isolated DNA bases as well as DNA polymers [47–49]. Metallic CNTs are therefore the natural choice for use in a nanopore device. However, semiconducting CNTs may be sufficiently conductive at room temperature to approximate metallic tubes. Furthermore, the sensitivity of transport in semiconducting CNTs to local electrostatic charge may be useful for probing the electrostatic properties of translocating molecules. The performance of transverse CNT probes, be they metallic or semiconducting, should be investigated experimentally.

6. Electrochemical characterization of an embedded electrode formed by TEM milling

The fabrication of nanopores with embedded electrodes by TEM milling may result in a deterioration of the electrical properties at the electrode surface. It is possible, for

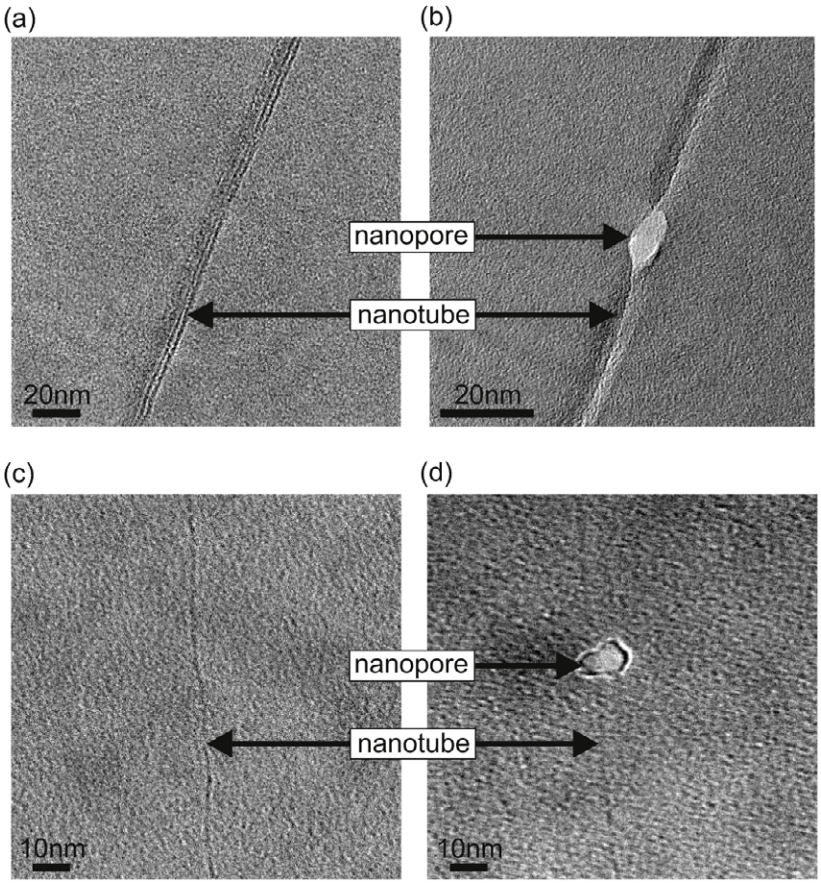

Figure 8. The fabrication of nanopores articulated with transverse CNT electrodes. Two sets of TEM images show a pair of embedded CNTs before ((a), (c)) and after ((b), (d)) the TEM-milled nanopores through the supporting membrane, bisecting the CNTs.

example, that the electron–atom collisions responsible for the formation of the pore also displace atoms from the mini-membrane into the electrode layer, or induce their inter-diffusion. Since conduction at the embedded electrode surfaces is of paramount importance to the operation of several envisioned nanopore devices, we have used cyclic voltammetry (CV) measurements to electrochemically verify that TEM milling preserves conduction in a TEM-milled, annular gold electrode inside an insulating nanopore. CV is highly sensitive to electrode–electrolyte interface because the solvated redox species must come into intimate contact with the electrode for the tunneling process to proceed.

We performed CV measurements to test the behavior of a patterned electrode in a gated nanopore device at the different stages of the fabrication illustrated in figures 9(a)–(d). At each stage, a fluid reservoir was created on the front side of a nanopore chip by sealing a silicone O-ring (inner diameter = 2 mm, outer diameter = 4 mm) around the membrane using polydimethylsiloxane (PDMS) as an adhesive. The reservoir was filled with a solution containing 0.5 mM $Fc(CH_2OH)_2$ (ferrocenedimethanol, Sigma-Aldrich), which served as the redox species, and 0.5 M NH_4NO_3 (ammonium nitrate, Sigma), a supporting electrolyte. An Ag/AgCl (3 M NaCl) standard reference electrode was immersed in the solution, along with a Pt wire, used as the counter electrode. The patterned metal layer deposited on the SiN membrane served as the working electrode. CV scans between 0.05 and 0.45 V were recorded with an electrochemical analyzer (CHI 600C, CH Instruments).

The deposition of Ti (2 nm)/Au (8 nm)/Ti (2 nm) patterned electrodes on the front surface of the device (figure 9(a)) created a large contact area ($\sim$0.3 mm^2) between the metal and the electrolyte, which was reflected in the large magnitude of the redox current peaks shown in figure 9(e). The heights of the reduction peak and the oxidation peak were i_{pr} = 205 nA and i_{po} = 240 nA, respectively, which agree well with the theoretical current peak height i_p = 237 nA, calculated from [50]:

$$i_p = (2.69 \times 10^5) Ac\sqrt{n^3 D\nu}, \tag{3}$$

where i_p is the peak current in amperes, A is the area of the exposed electrode in cm^2, c is the bulk concentration of the redox species in mol cm^{-3}, $n = 1$ is the number of electrons transferred in one redox reaction, $D = 6.9 \times 10^{-6}$ cm^2 s^{-1} is the diffusion coefficient of $Fc(CH_2OH)_2$ [51], and ν = 0.05 V s^{-1} was the scan rate.

The patterned electrode was insulated by depositing 20 nm of ALD Al_2O_3 (figure 9(b)), after which no redox peaks were observed in a CV scan at a rate of 0.5 mV s^{-1} (figure 9(f)). The observed 1.2 pA gap between the forward and backward scans is in perfect agreement with the expected capacitive charging of the dielectric layer in series with the electric double layer, which is calculated from:

$$2 \times I = 2 \times CA\nu = 1.2\,\text{pA}, \tag{4}$$

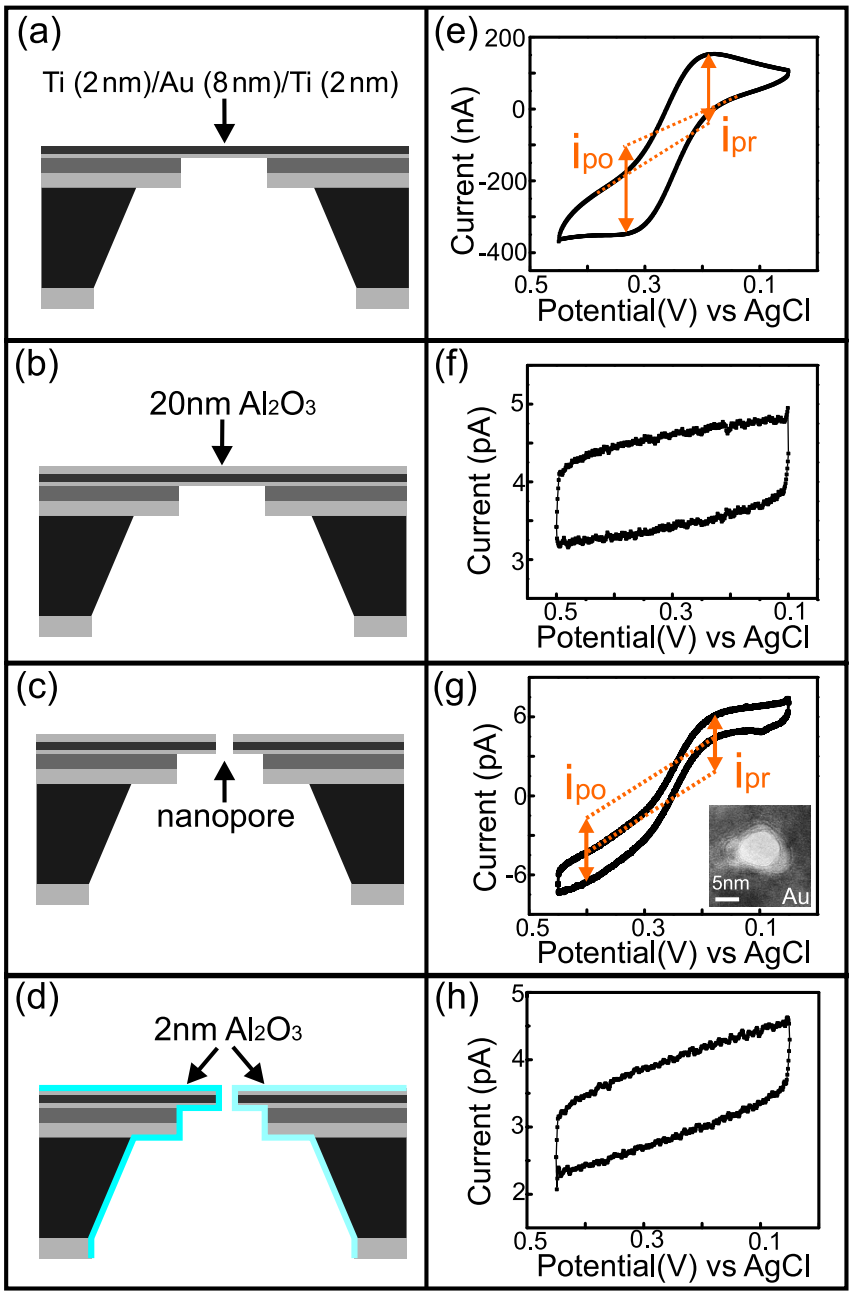

Figure 9. Cyclic voltammetry measurements of a patterned gold working electrode at various stages of its integration into a gated nanopore device, relative to Ag/AgCl in 0.5 mM $Fc(CH_2OH)_2$ in 0.5 M NH_4NO_3. The patterned electrode was tested: (a) after depositing the Ti (2 nm)/Au (8 nm)/Ti (2 nm) patterned electrode on the front surface of the nanopore chip; (b) after insulating the electrode with 20 nm of ALD Al_2O_3; (c) after milling an 8 nm wide nanopore through the stack of materials by TEM; (d) after the annular gate electrode was covered by an additional 2 nm of ALD Al_2O_3. Panels (e)–(h) show the CV curves corresponding to stages (a)–(d), respectively. The results demonstrate that the electrochemically active electrode (a) was fully passivated by the 20 nm ALD dielectric coating (b), and that TEM milling revealed an active annular electrode on the inner pore surface (c), which was well insulated by the second ALD coating. The inset of (g) shows the 8 nm diameter nanopore tested.

where the capacitance of the interface C is obtained from the specific capacitance 0.4 μF cm^{-2} of the 20 nm thick Al_2O_3 layer [52], in series with the specific capacitance of the electric double layer, which is typically $\sim$20 μF cm^{-2} [53].

An 8 nm wide nanopore was milled through the mini-membrane by TEM, exposing an annular metal electrode on the inner surface of the pore (figure 9(c)). The corresponding CV curve, obtained at a scan rate of 0.5 mV s^{-1}, is shown in figure 9(g). The heights of the reduction peak and the oxidation peak were 4.2 pA and 4.8 pA, respectively, which are in good agreement with the 4.1 pA value that was predicted based on the following calculation. The Comsol Multiphysics simulation package was used to numerically solve the Nernst–Planck equation for the distribution of redox species in the nanopore geometry, and then to calculate the electrochemical current based on the diffusive flux of the redox species into the

annular electrode, as described by Fick's law. The details of this simulation are described in the appendix.

The embedded gate electrode was insulated by depositing an additional 2 nm of ALD Al_2O_3 (figure 9(d)), which covered the electrode without closing the nanopore. The corresponding CV curve (figure 9(h)), scanned at a rate of 0.5 mV s^{-1}, again shows no redox peaks, and a current gap of 1.2 pA between the forward and backward scans, as was the case in figure 9(f).

We have performed ionic current gating measurements using nanopore devices that were made by the FIB and the TEM methods. In all devices, an embedded annular gate electrode was coated with an insulating layer of ALD Al_2O_3. The results of our experiments, which will be reported in detail elsewhere, show that the ionic conductance through the nanopore can indeed be modulated by a field effect, and that the response is strongly influenced by the surface chemistry, as predicted [5]. The useful range of the applied gate field was found to be limited by the dielectric strength of the insulating Al_2O_3 layer. In some devices, no gating effects were observed, which was possibly due to broken electrical connections to the perimeter of the gate electrode.

7. Conclusions

The fabrication of nanopores with a single annular gate electrode, or with two transverse CNT nanoelectrodes, has been demonstrated. The approach is based on milling through electrodes embedded in a freestanding membrane using either FIB or TEM. Milling and imaging capabilities are thereby combined, which makes the alignment of nanopores and nanoelectrodes relatively straightforward. FIB milling is fast, and can easily define a nanopore with a regular perimeter in any material, although the spatial resolution is limited to tens of nanometers. However, ALD coatings can insulate the electrode surface, and shrink the pore to the desired final diameter with nanometer accuracy. Milling at single nanometer spatial resolution requires a TEM, whose electron beam mills light elements optimally because sputtering is the dominant mechanism, as we have shown. Furthermore, electrochemical measurements on a TEM-milled electrode confirmed that its electrical properties were preserved.

The nanopore devices we have demonstrated here can implement new single-molecule manipulation and detection strategies. The gated nanopore devices with embedded annular electrodes were designed to control DNA translocations via an electrostatic field effect. The method for fabricating transverse CNT electrodes outlined here may, with some refinement, produce nanopore devices capable of probing the local electronic properties of translocating molecules.

Acknowledgments

Zhijun Jiang acknowledges support from the National Science Foundation through a Rhode Island EPSCoR Graduate Student Fellowship. Mirna Mihovilovic acknowledges support from Intel Corporation. This work was supported by the NSF under grant DMR-0805176.

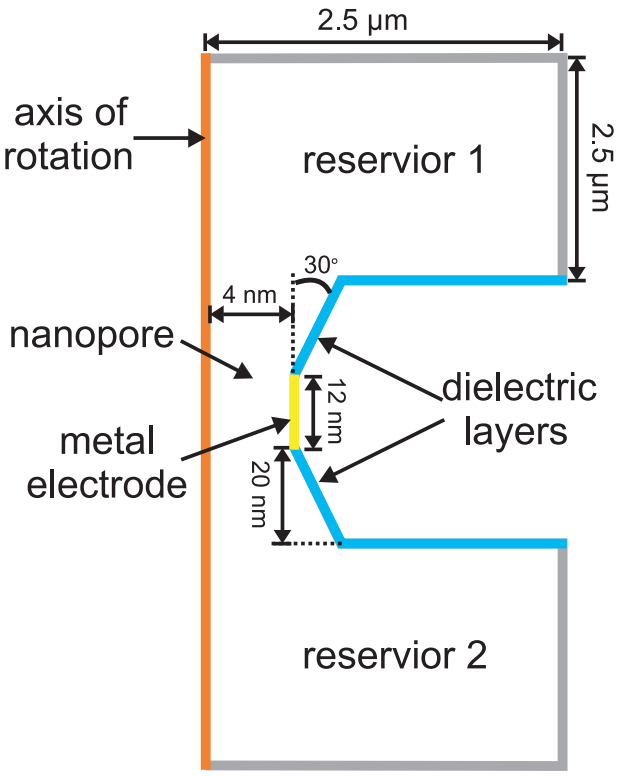

Figure A.1. Cross-section of one half of the cylindrically symmetric nanopore geometry in which the distribution of redox species was modeled using Comsol multiphysics. The sketch illustrates the surface of the metal layer, the axis of rotation used to obtain the 3D nanopore geometry, the boundaries of the two reservoirs and the dielectric coating of the nanopore. The concentration of redox species was fixed at 0.5 mM at the top boundary of reservoir 1 and the bottom boundary of reservoir 2, and it was fixed at 0 mM at the surface of the metal layer.

Appendix

Simulations of the distribution of redox species in the nanopore were performed with Comsol Multiphysics (3.2a) using the Electrostatic Module (which implements the Poisson equation) and the Nernst–Planck without electroneutrality module. A two-dimensional cylindrically symmetric nanopore geometry was modeled for computational efficiency. Figure A.1 shows the geometry of the nanopore with a 12 nm thick, embedded annular electrode, flanked on either side by large reservoirs. This pore geometry approximates the truncated double-cone structure of the nanopore revealed by the electron microscope tomography measurements by Kim *et al* [41]. The maximum mesh sizes were set to 10 nm in the reservoirs, 1 nm near the two insulating layers inside the nanopore and 1 Å at the metal layer. The governing diffusion equation for the distribution of redox species is:

$$\frac{\partial c}{\partial t} = D \bigtriangledown^2 c. \qquad \text{(A.1)}$$

The redox concentration was set to 0 mM at the surface of the metal layer. The potential at the metal surface was set to 0.18 and 0.40 V in two separate runs to match the potentials of the metal electrode where peak currents were observed in our experiments (figure 9(g)). The redox concentration was

fixed at 0.5 mM and the potential was fixed at ground at the top boundary of the upper reservoir and the bottom boundary of the lower reservoir. The DIRECT (UMFPACK) time independent solver was used. The average concentration gradient of the redox species at the surface of the metal layer was calculated to be 0.206 and 0.208 mM nm^{-1} for the two potential settings of the metal electrode 0.18 V and 0.4 V, respectively. Fick's law then gives the expected redox peak current according to:

$$i_p = -FDA'\nabla c, \tag{A.2}$$

where A' is the area of the exposed metal on the inner wall of the nanopore. From equation (A.2), our simulations predict a peak current of 4.1 pA.

References

[1] Li J, Stein D, McMullan C, Branton D, Aziz M J and Golovchenko J A 2001 *Nature* **412** 166–9
[2] Schoch R B and Renaud P 2005 *Appl. Phys. Lett.* **86** 253111
[3] Karnik R, Fan R, Yue M, Li D, Yang P and Majumdar A 2005 *Nano Lett.* **5** 943–8
[4] Nam S W, Rooks M J, Kim K B and Rossnagel S M 2009 *Nano Lett.* **9** 2044–8
[5] Jiang Z and Stein D 2010 *Langmuir* **26** 8161–73
[6] Branton D, Golovchenko J A and Denison T J 2003 *US Patent Specification* 6627067
[7] Li J, Stein D, Schurmann G M, King G M, Golovchenko J, Branton D and Aziz M 2007 *US Patent Specification* 7258838
[8] Zwolak M and Di Ventra M 2005 *Nano Lett.* **5** 421–4
[9] Lagerqvist J, Zwolak M and Di Ventra M 2006 *Nano Lett.* **6** 779–82
[10] He J, Lin L, Zhang P, Spadola Q, Xi Z, Fu Q and Lindsay S 2008 *Nano Lett.* **8** 2530–4
[11] Zandbergen H W, van Duuren R J H A, Alkemade P F A, Lientschnig G, Vasquez O, Dekker C and Tichelaar F D 2005 *Nano Lett.* **5** 549–53
[12] Gracheva M E, Xiong A, Aksimentiev A, Schulten K, Timp G and Leburton J P 2006 *Nanotechnology* **17** 622–33
[13] Fischbein M D and Drndić M 2007 *Nano Lett.* **7** 1329–37
[14] Fischbein M D and Drndić M 2009 *Appl. Phys. Lett.* **93** 113107
[15] Kalman E B, Sudre O, Vlassiouk I and Siwy Z S 2009 *Anal. Bioanal. Chem.* **394** 413–9
[16] Chen G S, Boothroyd C B and Humphreys C J 1998 *Phil. Mag.* A **78** 491–506
[17] Mochel M E, Eades J A, Metzger M, Meyer J I and Mochel J M 1984 *Appl. Phys. Lett.* **44** 502–4
[18] Storm A J, Chen J H, Ling X S, Zandbergen H W and Dekker C 2003 *Nat. Mater.* **2** 537–40
[19] Heng J B, Ho C, Kim T, Timp R, Aksimentiev A, Grinkova Y V, Sligar S, Schulten K and Timp G 2004 *Biophys. J.* **87** 2905–11
[20] McNally B, Wanunu M and Meller A 2008 *Nano Lett.* **8** 3418–22
[21] Krapf D, Wu M, Smeets R M M, Zandbergen H W, Dekker C and Lemay S G 2006 *Nano Lett.* **6** 105–9
[22] Gnaser H 1999 *Low-Energy Ion Irradiation of Solid Surfaces* (New York: Springer)
[23] Giannuzzi L A, Prenitzer B I and Kempshall B W 2005 *Introduction to Focused Ion Beams: Instrumentation, Theory, Techniques and Practice* ed L A Giannuzzi and F A Stevie (New York: Springer) p 30
[24] Leskela M and Ritala M 2002 *Thin Solid Films* **409** 138–46
[25] Chen P, Mitsui T, Farmer D B, Golovchenko J, Gordon R G and Branton D 2004 *Nano Lett.* **4** 1333–7
[26] Orloff J, Swanson L and Utlaut M W 2005 *High Resolution Focused Ion Beams: FIB and Applications* (New York: Springer) p 141 and p 137
[27] Landau L D and Lifshitz E M 1976 *Mechanics* 3rd edn (Oxford: Butterworth–Heinemann) p 47
[28] Cherns D 1977 *Phil. Mag.* **36** 1429–44
[29] Hiraki J, Mori H, Taguchi E, Yasuda H, Kinoshita H and Ohmae N 2005 *Appl. Phys. Lett.* **86** 223101
[30] Terrones M, Banhart F, Grobert N, Charlier J C, Terrones H and Ajayan P M 2002 *Phys. Rev. Lett.* **89** 075505
[31] Remeika M and Bezryadin A 2005 *Nanotechnology* **16** 1172–6
[32] Takeda S, Koto K, Lijima S and Ichihashi T 1997 *Phys. Rev. Lett.* **79** 2994–7
[33] Chen G S, Boothroyd C B and Humphreys C J 1993 *Appl. Phys. Lett.* **62** 1949–51
[34] Xu S, Tian M, Wang J, Xu J, Redwing J M and Chan M H W 2005 *Small* **1** 1221–9
[35] Iijima S and Ichihashi T 1986 *Phys. Rev. Lett.* **56** 616–9
[36] Mochel M E, Humphreys C J, Eades J A, Mochel J M and Petford A M 1983 *Appl. Phys. Lett.* **42** 392–4
[37] Yokota T, Murayama M and Howe J M 2003 *Phys. Rev. Lett.* **91** 265504
[38] Bysakh S, Shimojo M, Mitsuishi K and Furuya K J 2004 *J. Vac. Sci. Technol.* B **22** 2620–7
[39] Egerton R F, Li P and Malac M 2004 *Micron* **35** 399–409
[40] Storm A J, Chen J H, Ling X S, Zandbergen H W and Dekker C 2005 *J. Appl. Phys.* **98** 014307
[41] Kim M-J, Wanunu M, Bell C D and Meller A 2006 *Adv. Mater.* **18** 3149–53
[42] Hobbs L W 1979 *Introduction to Analytical Electron Microscopy* ed J J Hren, J I Goldstein and D C Joy (New York: Plenum) pp 437–76
[43] Williams D B and Carter C B 2004 *Transmission Electron Microscopy* vol 1 (New York: Springer) p 64
[44] Nastasi M, Mayer J W and Hirvonen J K 2004 *Ion–Solid Interactions: Fundamentals and Applications* (New York: Cambridge University Press) p 146
[45] Hamada N, Sawada S and Oshiyama A 1992 *Phys. Rev. Lett.* **68** 1579–81
[46] Branton D *et al* 2008 *Nat. Biotechnol.* **26** 1146–53
[47] Driscoll R J, Youngquist M G and Baldeschwieler J D 1990 *Nature* **346** 294–6
[48] Tao N J, DeRose J A and Lindsay S M 1993 *J. Phys. Chem.* **97** 910–9
[49] Shapir E, Cohen H, Calzolari A, Cavazzoni C, Ryndyk D A, Cuniberti G, Kotlyar A, Felice R D and Porath D 2008 *Nat. Mater.* **7** 68–74
[50] Bard A J and Faulkner L R 1980 *Electrochemical Methods: Fundamentals and Applications* (New York: Wiley) p 218
[51] Xiong H, Guo J, Kurihara K and Amemiya S 2004 *Electrochem. Commun.* **6** 615–20
[52] Shimada Y, Yamashita Y and Takamizawa H 1988 *IEEE Trans. Compon. Hybrids Manuf. Technol.* **11** 163–70
[53] Weng T and Teng H 2001 *J. Electrochem. Soc.* **148** A368–73